Journal of Materials Chemistry B

ROYAL SOCIETY OF CHEMISTRY

PAPER

View Article Online
View Journal | View Issue

Cite this: J. Mater. Chem. B, 2025, 13, 12502

Optimizing bio-imaging with computationally designed polymer nanoparticles

Anupom Roy[a] and Conrard Giresse Tetsassi Feugmo *[ab]

Conjugated polymer nanoparticles (CPNs), especially poly(*p*-phenylene ethynylene) nanoparticles (PPE-NPs), are promising candidates for bio-imaging due to their high photostability, adjustable optical characteristics, and biocompatibility. Despite their potential, the fluorescence mechanisms of these nanoparticles are not yet fully understood. In this work, we modeled a spherical PPE-NP in a water environment using 30 PPE dimer chains. Combining molecular dynamics (MD) simulations and time-dependent density functional theory (TD-DFT) calculations, we examined the structural and optical properties of PPE-NPs in water. The MD simulations showed that PPE-NPs remain stable *via* hydrophobic interactions, with octyloxy side chains shielding the core from water. After evaluating six hybrid functionals, we found that the M05 functional provided the most accurate prediction of absorption wavelengths (450.94 nm *vs.* the experimental value of 450.00 nm). TD-DFT analysis of selected PPE dimer chains revealed strong fluorescence, characterized by high oscillator strengths (2.689–4.004) and large Stokes shifts (134.51–156.31 nm), which minimize spectral overlap and improve imaging resolution. Highest occupied molecular orbitals (HOMO)–lowest unoccupied molecular orbitals (LUMO) orbital analysis confirmed that $\pi \rightarrow \pi^*$ transitions dominate (>90%), indicating efficient electronic behavior. These results reinforce the potential of PPE-NPs as effective fluorescent probes for bio-imaging, supported by a reliable computational approach for designing future CPNs. By comparing computational predictions with experimental data, this study contributes to the development of customized nanomaterials for biomedical applications.

Received 15th April 2025,
Accepted 28th August 2025

DOI: 10.1039/d5tb00890e

rsc.li/materials-b

1 Introduction

Biological imaging stands as a pivotal tool in contemporary biomedical research, providing critical insights into the cellular and molecular mechanisms that govern health and disease.[1] By allowing scientists to visualize and dissect the complex structures and dynamic behaviors of living systems, imaging technologies have transformed our comprehension of biology across various scales—ranging from individual molecules to whole organisms. Advanced imaging techniques have substantially enhanced our ability to investigate complex biological systems, thereby catalyzing significant advancements in diagnostics, therapeutics, and drug development.[2] Fluorescence imaging, in particular, has gained widespread recognition for its exceptional sensitivity, high resolution, and the capability to target specific biomolecules within living cells and tissues.[3,4] Nevertheless, conventional fluorescent dyes, despite their extensive application, are hindered by limitations such as photobleaching,[5] limited tunability,[6] and potential toxicity.[7] To address these shortcomings, conjugated polymer nanoparticles (CPNs) have emerged as a highly promising alternative, offering enhanced performance and versatility in biological imaging.[8] Among the diverse CPNs, poly(*p*-phenylene ethynylene) (PPE) has garnered significant attention due to its exceptional fluorescence efficiency, chemical stability, and highly tunable optical properties.[9,10] Reported photophysical studies show that water-soluble PPE derivatives exhibit a UV-vis absorption maximum around 434 nm, an emission maximum near 460 nm, and an absolute fluorescence quantum yield of approximately 19%.[11] In conjugated-polymer nanoparticles, PPE typically absorbs at ~390 nm and emits at ~440 nm, with a somewhat lower quantum yield of ~12%.[12] Structural modifications can further tune these properties; for example, mannose-coated PPE displays absorption at 393 nm and emission at 466.5 nm, accompanied by a large Stokes shift favorable for sensing applications.[13] Similarly, PPE nanoparticles functionalized with azide-terminated tetraethylene glycol (TEG) side chains achieve fluorescence quantum yields of ~13%, highlighting the versatility of PPE photophysics and its suitability for diverse optoelectronic and sensing applications.[9]

[a] Department of Chemistry, University of Waterloo, 200 University Ave. West, Waterloo, ON N2L 3G1, Canada. E-mail: cgtetsas@uwaterloo.ca
[b] Waterloo Institute for Nanotechnology, University of Waterloo, 200 University Ave. West, Waterloo, ON N2L 3G1, Canada

PPE is a conjugated polymer with a distinctive chemical structure composed of alternating phenylene and ethynylene units in its backbone.[9] This rigid-rod polymer is known for its semiconductive properties and efficient excited-state migration, making it a highly promising material for a variety of applications.[14] The backbone of PPE consists of benzene rings (phenylene groups) connected by carbon–carbon triple bonds (ethynylene groups), which confer several important characteristics. These include extended π-conjugation along the polymer chain, high fluorescence quantum yields (with some derivatives exceeding 90% in methanol), and efficient exciton migration, which enables potential signal amplification in sensory systems.[15] PPE is typically synthesized through Sonogashira–Hagihara coupling polymerization, a palladium-catalyzed reaction between aromatic diiodo compounds and diethynyl monomers.[16] By varying the synthesis process, different side chains and functionalities can be incorporated, allowing the properties of PPE to be tailored for specific applications. This versatility has led to its exploration in a wide range of fields.

PPEs have shown significant promise in several areas. For chemical sensors, their ability to produce signal amplification makes them highly effective for detecting various analytes.[17] In biosensors, water-soluble PPE derivatives with cationic groups have been developed, enabling their use in biological environments.[15] The conjugated structure of PPEs also makes them suitable for optoelectronic devices, where their electronic properties can be harnessed. Additionally, the introduction of boron clusters into PPE has been shown to enhance its heat resistance, expanding its potential use in high-temperature applications.[16] Researchers are actively working to enhance PPE's properties and broaden its functionality. For example, on-surface synthesis of PPE molecular wires has been achieved under ultra-high vacuum conditions, opening new possibilities for nanoscale applications.[18] Water-soluble PPE derivatives with cationic trimethyl phosphonium moieties have also been developed, showing promise for biosensing and biocidal applications.[15] Furthermore, studies on the mechanical properties of PPE have revealed that mechanical stress can cleave the $sp–sp^2$ bond, with bond dissociation energy reaching up to 600 kJ mol^{-1}.[19]

Computational methodologies, including density functional theory (DFT) calculations[20] and molecular dynamics (MD)[21] simulations, are of significant importance and utility in probing the fluorescence properties of conjugated polymer nanoparticles (CPNs), such as poly(*p*-phenylene ethynylene) (PPE). These methodologies confer several key advantages concerning predictive capacity, comprehension of structure–property interrelations, optimization and design, as well as elucidation of complex phenomena. DFT calculations constitute a potent and cost-effective approach to uncovering fundamental material information, encompassing aspects such as energy, geometric structure, and electrical and optical characteristics.[22] MD simulations can elucidate energy transfer processes within CPNs, which is vital for the design of efficient fluorescent probes.[23] These methodologies yield significant theoretical forecasts and support within the realm of material design, providing substantial insights at the atomic, molecular, and unit cell levels.[22] This predictive capability is particularly advantageous in the investigation of CPNs, where an in-depth comprehension of the interrelation between molecular structure and fluorescence characteristics is imperative.

This research constitutes a thorough computational study on the optical characteristics of poly(*p*-phenylene ethynylene) nanoparticles (PPE-NPs) as bio-imaging probes. Addressing the limited exploration of computational methodologies in this domain, the study integrates time-dependent density functional theory (TDDFT) calculations with molecular dynamics (MD) simulations to forecast the optical properties of PPE-NPs of varying sizes. To ensure the accuracy of our findings, computational predictions are corroborated with experimental data. This investigation not only yields significant insights into the structure–property relationships of PPE-NPs but also highlights their potential as sophisticated probes in bio-imaging applications.

2 Computational methods

2.1 Structure preparation

In this study, we employed the poly(*p*-phenylene ethynylene) (PPE) polymer featuring a phenylene ethynylene backbone and octyloxy side chains, as illustrated in Fig. 1. A PPE dimer molecule, consisting of six phenylene ethynylene rings and eight octyloxy side chains, was built utilizing DrawMol software packages.[24] The initial geometry optimization of the individual PPE dimer molecule was conducted employing the B3LYP/6-31G* computational method within the polarizable continuum model (PCM) framework, utilizing the integral equation formalism variant (IEFPCM) with water as the solvent.[25] This optimization process was executed using the Gaussian 16 software.[26] Subsequently, a PPE nanoparticle was created using the Packmol package.[27] The nanoparticle, shaped as a sphere with a 3.5 nm radius, consists of 30 PPE dimer molecules, as depicted in Fig. 2. This spherical nanoparticle system was then utilized for molecular dynamics (MD) simulations. The choice of 30 dimer chains was made to balance physical relevance with computational feasibility. While experimentally reported PPE nanoparticles often exceed 20 nm in diameter,[9,10] modeling

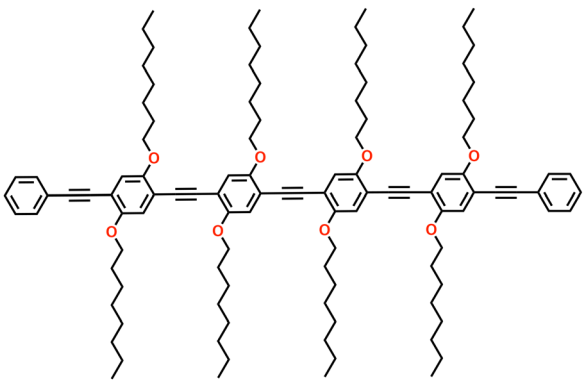

Fig. 1 Molecular structure of a dimer molecule of PPE.

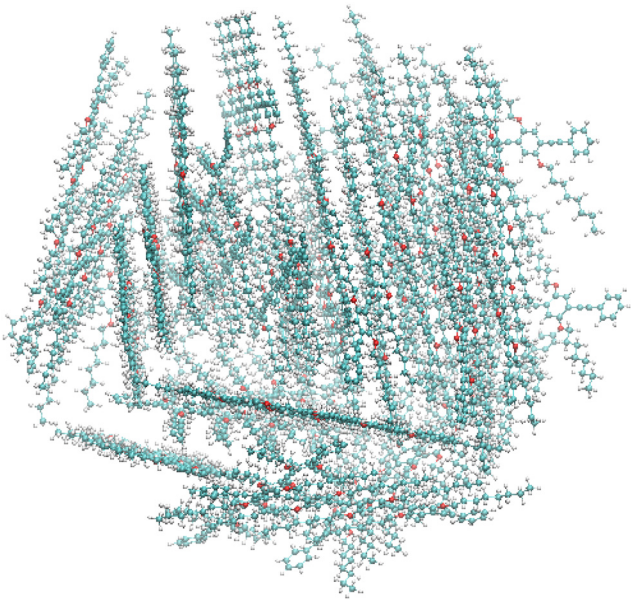

Fig. 2 Illustration depicts the nanoparticle consists of 30 PPE dimer molecule.

such large systems with all-atom MD is prohibitively expensive. The selected system, comprising 30 dimers with a radius of 3.5 nm, is computationally feasible. Despite the smaller size, this model captures critical characteristics observed in experiments, such as stable self-aggregation, formation of a compact hydrophobic core, and solvation of octyloxy side chains at the water interface. These structural features were essential to probe the fundamental photophysical behavior of PPE-NPs at the molecular level.

2.2 Molecular dynamics (MD) simulation

The Restrained ElectroStatic Potential (RESP) charges[28] were computed using the Gaussian 16 program at the IEFPCM(water)-B3LYP/6-31G* level of theory. The electrostatic potential (ESP) was fitted to the van der Waals surface grid using the Merz–Singh–Kollman (MK) scheme[29] for parameterization. The spherical nanoparticle system was placed in a 10 × 10 nm water box, with water molecules excluded from the nanoparticles core. The solvated system was first energy-minimized using the steepest descent algorithm[30] until the maximum force on any atom fell below 1000.0 kJ mol^{-1} nm^{-1}. Following this, equilibration was performed using the NVT (constant number of atoms, volume, and temperature) and NPT (constant number of atoms, pressure, and temperature) ensembles at 300 K and 1 bar. Temperature coupling was achieved using the V-rescale thermostat, while pressure coupling at 1 bar was managed with the Parrinello–Rahman method[31] and semi-isotropic scaling. Simulations were conducted under periodic boundary conditions (PBC), with electrostatic interactions handled by the particle mesh Ewald (PME) method.[32] A force-switch cutoff was applied to the Lennard-Jones potential within the range of 1.0–1.2 nm. The production run was conducted using both NVT and NPT ensembles at a temperature of 300 K and a pressure of 1 bar. The time step was set to 2 fs, and the simulation duration was 4 microseconds. The GROMACS 2023 package,[33–35] combined with the OPLS-AA force field,[36] was used for molecular dynamics (MD) simulations. The system topology and coordinates were generated using the CHARMM-GUI platform.[37]

2.3 Time-dependent density functional theory (TD-DFT) calculations for benchmarking

The equilibrated structure of a single PPE dimer was derived from molecular dynamics (MD) simulations. This structure was then used to perform excited state time-dependent density functional theory (TD-DFT) single point energy calculations, considering 10 excited states. These calculations computed vertical excitation wavelengths, excitation energies, oscillator strengths, HOMO and LUMO energies, HOMO–LUMO gap, and HOMO–LUMO contribution percentages.

To identify the most suitable hybrid functional for accurately predicting the optical properties of PPE systems, we performed an extensive benchmarking using six widely used hybrid functionals: B3LYP,[38,39] ωB97XD,[40] CAM-B3LYP,[41] M05,[42] M062X,[43] and M11.[44] All calculations were performed with the 6-31G(d,p) basis set and the IEFPCM solvation model (water). These functionals were selected based on their established use in excited-state TD-DFT studies of organic and conjugated systems. The results of this benchmarking, including excitation wavelengths, oscillator strengths, HOMO–LUMO energies, and comparison with experimental data, are discussed in results and discussion section. Based on this analysis, the M05 functional was selected for all subsequent TD-DFT calculations of absorption and emission properties.

2.4 TD-DFT calculations for fluorescence properties of PPE nanoparticle

2.4.1 Absorption. After 4 μs of MD simulation of the PPE-NP in water, individual PPE dimer chains were extracted. These chains were not further geometry-optimized in order to preserve the equilibrated structural configuration of the nanoparticle. The extracted structures were treated as being in the ground electronic state (S_0). TD-DFT single-point excited-state calculations were then performed at the IEFPCM(water), TD-M05/6-31G(d,p) level of theory, considering 10 singlet excited states. From these calculations, vertical excitation wavelengths, excitation energies, oscillator strengths, HOMO and LUMO energies, HOMO–LUMO gap, and HOMO–LUMO contribution percentages were obtained to characterize the absorption properties.

2.4.2 Emission. From the set of 30 PPE dimer chains, 10 chains with absorption wavelengths closest to the experimental value were selected for emission analysis. For each of these chains, excited-state geometry optimization was performed in the first singlet excited state (S_1) using the same level of theory: IEFPCM(water), TD-M05/6-31G(d,p). Following optimization, TD-DFT single-point excited-state calculations (with 10 singlet excited states) were carried out on the S_1-optimized geometries. These calculations yielded vertical emission wavelengths,

excitation energies, oscillator strengths, HOMO and LUMO energies, HOMO–LUMO gap, and HOMO–LUMO contribution percentages, which were used to characterize the emission properties.

3 Results and discussions

3.1 MD results

We conducted extensive MD simulations on a PPE nanoparticle sphere solvated in water for 4 microseconds. The simulations revealed that the nanoparticle, composed of 30 PPE dimer chains, underwent conformational changes over time. Fig. 3 and SI Fig. S1–S5 illustrate these structural changes in the nanoparticle and individual PPE chains, respectively. Initially, all PPE chains had a planar structure, even within the nanoparticle, resulting in a non-uniform spherical shape. However, during the simulation, the chains rearranged through van der Waals and electrostatic interactions, forming a more uniform spherical structure. The phenylene ethynylene rings of the PPE dimer chains bent slightly, while the octyloxy side chains adopted various conformations to stabilize the nanoparticles spherical shape. Additionally, the nanoparticle reached equilibrium, as no major structural changes were observed at 2000, 3000, and 4000 ns. As described in the computational methods, no water molecules were initially placed inside the nanoparticles core during solvation; instead, they were positioned at least 2 Å away to test for penetration. Despite interactions between water and the nanoparticles outer layer, no water entered the core, as shown in Fig. 4, likely due to the hydrophobic nature of the octyloxy side chains.

Although the final simulated nanoparticle has a diameter of 3.2 nm, which is smaller than typical experimental PPE-NPs (>20 nm), the system reproduces essential features of

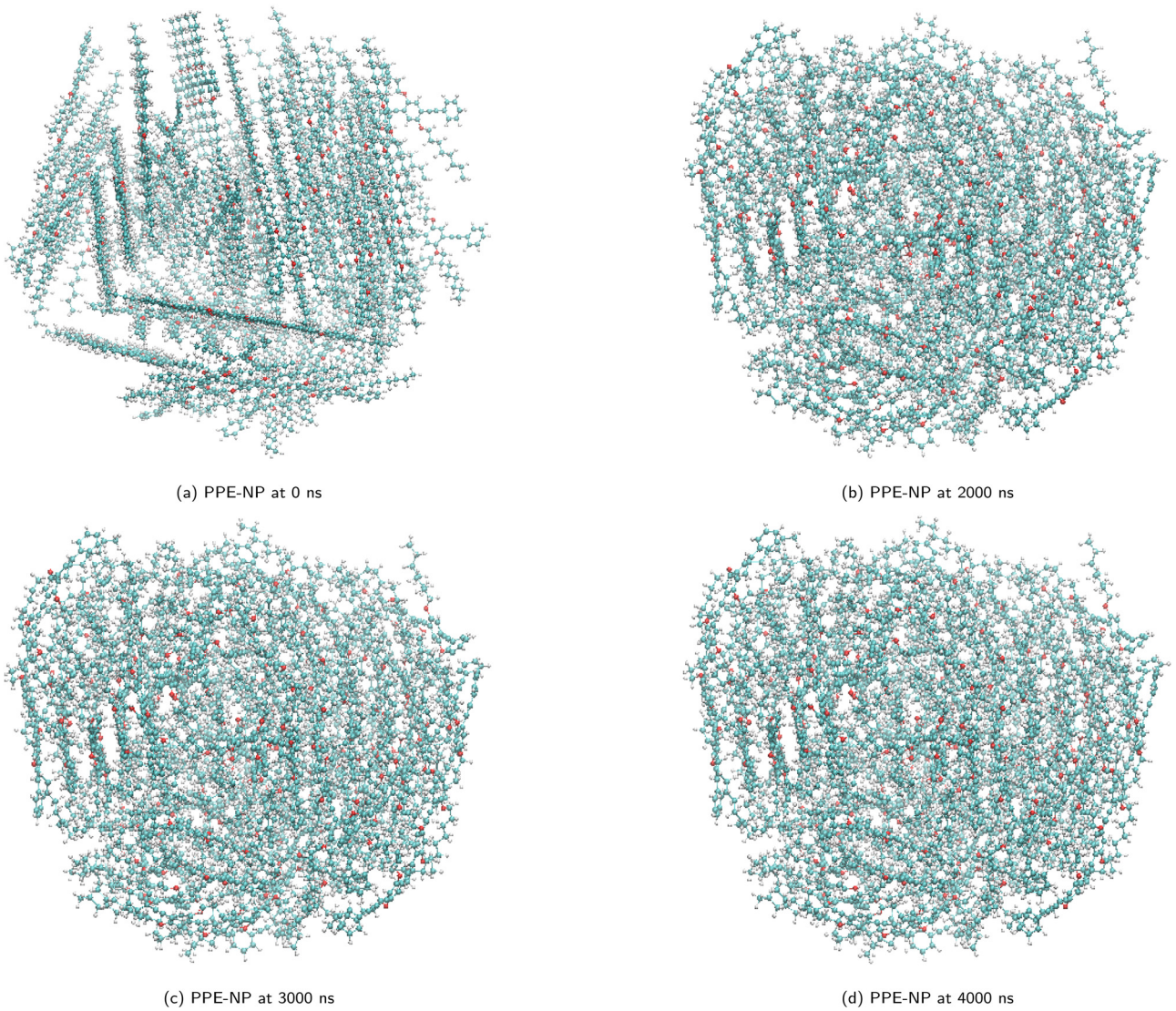

Fig. 3 Illustration depicts the conformational changes of the PPE nanoparticles: (a) at 0 ns, (b) at 2000 ns, (c) at 3000 ns, (d) at 4000 ns of the MD simulations.

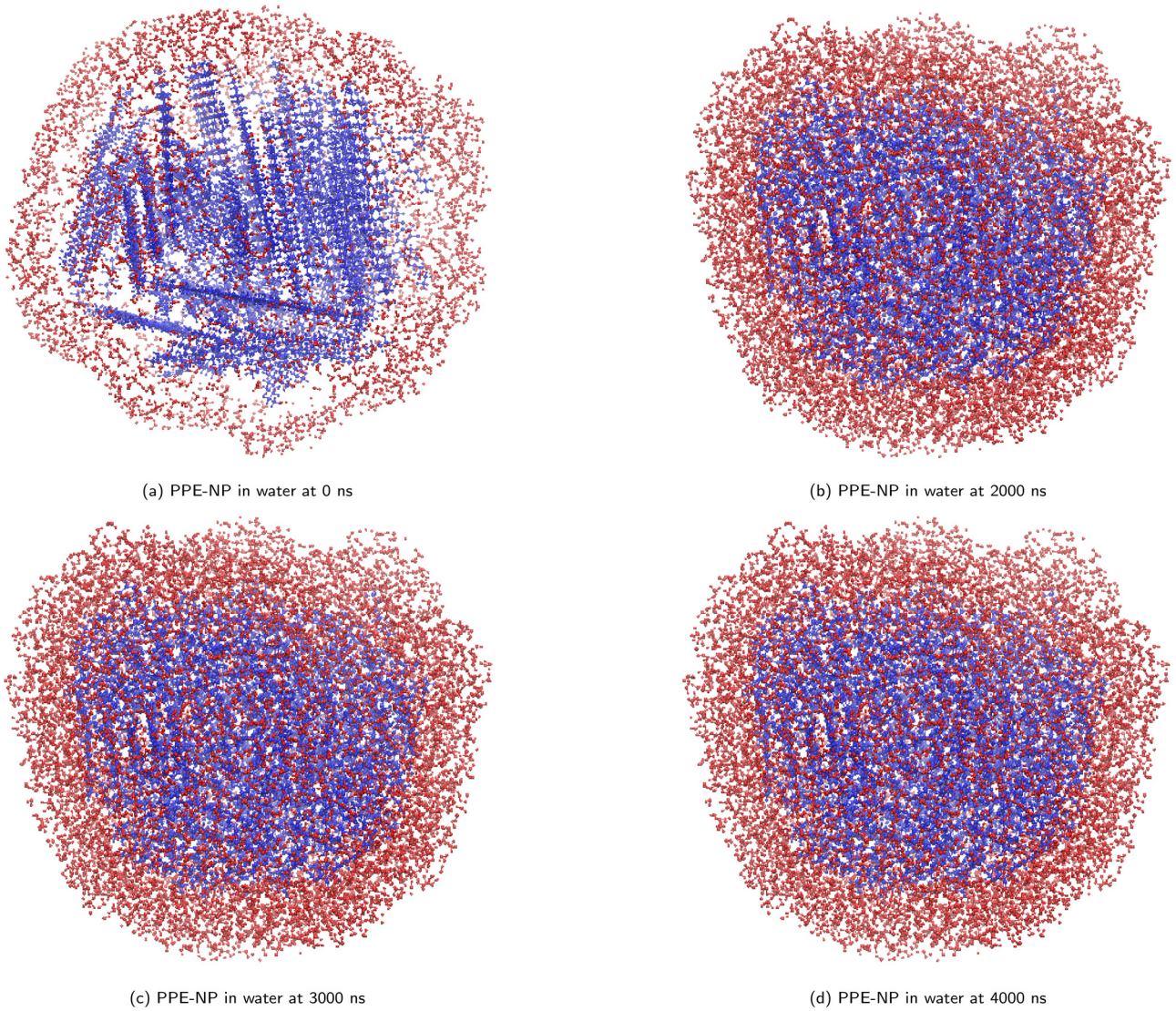

Fig. 4 Illustrations depicts the water distribution of the PPE nanoparticles, with PPE atoms represented in blue, while water molecules are depicted in red: (a) at 0 ns, (b) at 2000 ns, (c) at 3000 ns, (d) at 4000 ns of the MD simulations.

nanoparticle self-assembly. Specifically, the simulation confirms the formation of a stable spherical aggregate with a well-defined hydrophobic interior and water-exposed octyloxy side chains, consistent with the amphiphilic behavior of PPE polymers. The reduced system size allowed for detailed atomistic analysis of structure–function relationships while remaining computationally tractable. These results validate the use of the 30-dimer model as a representative system for studying PPE-NP photophysics *in silico*.

3.2 Benchmarking

To computationally study the fluorescence properties of PPE nanoparticles and/or chains, selecting an appropriate functional that accurately predicts vertical excitation wavelengths compared to experimental data is essential. In this work, six hybrid functionals—B3LYP, ωB97XD, CAM-B3LYP, M05, M062X, and M11—were benchmarked using Gaussian TD-DFT calculations to compare absorption wavelengths with experimental[9] values. A single PPE dimer chain extracted from MD simulations was analyzed. As detailed in the methods, excitation wavelengths, energies, oscillator strengths, and HOMO–LUMO data were computed with the 6-31G(d,p) basis set and IEFPCM(water) solvation, as presented in Table 1.

The vertical excitation length (wavelength) and the corresponding excitation energy are crucial in determining the absorption characteristics of the PPE dimer molecule. the experimental value of PPE nanoparticle for the vertical excitation length is 450.00 nm, which corresponds to an energy of ~2.76 eV. Among the functionals used M05 with 450.94 nm and 2.75 eV values for vertical excitation length and energy, respectively, shows the closest match to the experimental excitation wavelength. This indicates that M05 provides an accurate description of the electronic transition responsible for absorption. B3LYP with vertical excitation wavelength of

Table 1 The table shows the vertical excitation lengths (compared with experimental[9] value), vertical excitation energies oscillator strengths, HOMO–LUMO contribution percentages, HOMO energies, LUMO energies, and HOMO–LUMO energy gaps for the highest-energy excited state of a selected PPE dimer chain, performed at the TD-DFT level with different hybrid functionals and the 6-31(d,p) basis set

	B3LYP	ωB97XD	CAM-B3LYP	M05	M062X	M11	Experiment[9]
Vertical excitation length (nm)	471.11	384.88	391.89	450.94	388.53	363.01	450.00
Vertical excitation energy (eV)	2.632	3.221	3.164	2.750	3.191	3.415	—
Oscillator strength (f)	2.918	3.414	3.402	3.058	3.501	3.443	—
HOMO–LUMO contribution (%)	95.85	70.10	74.59	88.65	77.81	67.90	—
HOMO energy (eV)	−5.321	−7.152	−6.554	−5.632	−6.602	−7.674	—
LUMO energy (eV)	−2.198	−0.677	−1.158	−2.048	−1.573	−0.653	—
HOMO–LUMO energy gap (eV)	3.123	6.475	5.396	3.584	5.029	7.021	—

471.11 nm and vertical excitation energy of 2.63 eV overestimates the excitation wavelength, meaning it predicts a lower energy transition than observed experimentally. The range-separated functionals ωB97XD (with vertical excitation wavelength of 384.88 nm and vertical excitation energy of 3.22 eV), CAM-B3LYP (with vertical excitation wavelength of 391.89 nm and vertical excitation energy of 3.16 eV), and M11 (with vertical excitation wavelength of 363.01 nm and vertical excitation energy of 3.41 eV) predict much higher excitation energies, suggesting they introduce excessive charge transfer corrections. M062X (with vertical excitation wavelength 388.53 nm and vertical excitation energy of 3.19 eV), on the other hand, underestimates the wavelength, but not as significantly as M11.

The oscillator strength measures the intensity of the transition. A higher oscillator strength indicates a stronger absorption. All functionals predict relatively high oscillator strengths, ranging from 2.918 (B3LYP) to 3.501 (M062X). The strongest absorption is predicted by M062X (3.501), followed closely by ωB97XD (3.414), CAM-B3LYP (3.402), and M11 (3.443), indicating that these functionals predict intense electronic transitions. M05 (3.058) and B3LYP (2.918) predict slightly lower absorption strengths.

HOMO–LUMO contribution (%) describes how much of the transition comes from the HOMO → LUMO transition. A higher contribution suggests a simple and direct transition. B3LYP (95.85%) and M05 (88.65%) predict transitions that are almost entirely dominated by HOMO → LUMO contributions, making the transitions well-defined. M062X (77.81%) and CAM-B3LYP (74.59%) show moderate contribution. ωB97XD (70.10%) and M11 (67.90%) have the lowest contributions, indicating significant multi-configurational effects or charge-transfer character.

The HOMO energy reflects a molecules tendency to donate electrons, while the LUMO energy indicates its capacity to accept electrons. Among the functionals evaluated, M11 (−7.674 eV) predicts the lowest (most stabilized) HOMO energy, followed by ωB97XD (−7.152 eV), suggesting these functionals describe a reduced electron-donating tendency for the PPE dimer. In contrast, B3LYP (−5.321 eV) and M05 (−5.632 eV) yield relatively higher HOMO energies, implying a greater propensity for electron donation. Regarding LUMO energies, M11 (−0.653 eV) and ωB97XD (−0.677 eV) predict the least stabilized LUMOs, which could indicate less favorable conditions for charge transfer. On the other hand, B3LYP (−2.198 eV) and M05 (−2.048 eV) yield more stabilized LUMO energies, potentially supporting more efficient electron-accepting behavior.

A smaller HOMO–LUMO gap typically suggests strong absorption and lower excitation energy. B3LYP (3.123 eV) and M05 (3.584 eV) predict the smallest gaps, which correlate well with their longer excitation wavelengths. M11 (7.021 eV) and ωB97XD (6.475 eV) predict the largest gaps, resulting in significantly blue-shifted absorption (shorter wavelengths, higher energies). CAM-B3LYP (5.396 eV) and M062X (5.029 eV) show moderate gaps.

Overall, M05 is the best-performing functional because it provides the closest match to the experimental excitation wavelength (450.94 nm *vs.* 450.00 nm), a moderate HOMO–LUMO gap (3.584 eV), and a reasonable oscillator strength (3.058). Therefore, M05 functional with 6-31G(d,p) basis set and IEFPCM(water) environment was selected to use in further calculations for investigating fluorescence property of PPE nanoparticle in this study. On the other hand, M11 performs poorly in predicting vertical excitation wavelength (363.01 nm, heavily blue-shifted) and has a very high HOMO–LUMO gap (7.021 eV), making it unsuitable for describing absorption in the PPE dimer molecule.

3.3 Fluorescence properties of PPE

As described in the method section, for absorption properties, all 30 PPE dimer chains were extracted from the 4-microsecond MD simulations. These extracted chains represented a well-equilibrated structural configuration of the nanoparticle. To preserve the nanoparticles structural confirmation, the extracted chains were not further optimized to ground state. Instead, their structures were considered the ground state geometry (S_0) of PPE chains. We then performed TD-DFT single-point excited-state calculations at the IEFPCM(water), TD-M05/6-31G(d,p) level of theory, considering 10 singlet excited states. These calculations determined vertical excitation wavelengths, energies, oscillator strengths, and HOMO–LUMO contributions for absorption properties, as summarized in Table S1 in the SI.

For emission properties, we selected 9 PPE dimer chains whose absorption wavelengths were close to the experimental absorption wavelength (450.00 nm). These selected chains are as follows: 6, 7, 11, 18, 20, 23, 28, 29, and 30. These selected chains were further excited state geometry optimized in the

first singlet excited state (S_1) using the IEFPCM(water), TD-M05/6-31G(d,p) level of theory. Following optimization, TD-DFT single-point excited-state calculations (with 10 singlet excited states) were carried out on the S_1-optimized geometries. To analyze the fluorescence properties of these chains, we computed their vertical excitation wavelengths, excitation energies, oscillator strengths, HOMO–LUMO contributions, HOMO energies, LUMO energies, and HOMO–LUMO gaps for both absorption and emission (highest-energy excited state), as summarized in table.

3.3.1 Vertical excitation length. The vertical excitation length corresponds to the absorption wavelength of each PPE chain, and its variation provides insight into the electronic structure and conjugation effects in these systems. The absorption wavelengths range from 441.75 nm (Chain 11) to 460.95 nm (Chain 29), with most values clustering around 445–450 nm, which is close to the experimental absorption wavelength of 450.00 nm. A longer excitation wavelength (red-shifted absorption) generally indicates that the energy required for electronic excitation is lower, often due to an extended π-conjugation system or reduced electron localization. This is evident in Chain 29 (460.95 nm) and Chain 7 (454.12 nm), which show the longest excitation wavelengths, suggesting a more delocalized electron distribution. Conversely, shorter excitation wavelengths (blue-shifted absorption) indicate higher excitation energy, as seen in Chain 11 (441.75 nm), which might result from structural factors limiting delocalization. In fluorescence emission, the excitation wavelengths range from 582.17 nm (Chain 18) to 603.76 nm (Chain 29), compared to the experimental emission of 579.00 nm. The red shift in emission compared to absorption, known as the Stokes shift, arises due to molecular relaxation and solvation effects, stabilizing the excited state before photon emission. The computed emission range (582–604 nm) is slightly red-shifted compared to the experimental value (579 nm). This small discrepancy is within the known uncertainty range for TD-DFT methods and may result from limited excited-state sampling and simplified modeling of the full nanoparticle environment.

3.3.2 Vertical excitation energy. The excitation energies in absorption vary between 2.6897 eV (Chain 29) and 2.8066 eV (Chain 11). Chain 29 has the lowest excitation energy, corresponding to the longest excitation wavelength (460.95 nm), indicating a smaller HOMO–LUMO energy gap. This suggests that Chain 29 has a more extended π-conjugation system, leading to lower electronic transition energy. On the other hand, Chain 11, with the highest excitation energy (2.8066 eV), has the shortest excitation wavelength (441.75 nm), implying that a larger HOMO–LUMO gap requires more energy for excitation. Similarly, in fluorescence emission, the excitation energy ranges from 2.0535 eV (Chain 29) to 2.1297 eV (Chain 18), showing a general trend where fluorescence emission energies are lower than their corresponding absorption energies. This reduction in energy arises from structural reorganization in the excited state and solvation effects that stabilize the emitting configuration prior to photon emission.

3.3.3 Oscillator strength. The oscillator strength (*f*) is a measure of the probability of an electronic transition occurring, with higher values indicating stronger absorption and fluorescence intensity. The oscillator strengths for absorption range from 2.6891 (Chain 30) to 3.2409 (Chain 28). A high oscillator strength means that the transition dipole moment is significant, resulting in strong electronic transitions and intense absorption peaks. Chain 28 (3.2409) and Chain 18 (3.1397) have the highest oscillator strengths, indicating that these chains exhibit strong absorption and efficient electronic transitions. In fluorescence emission, the oscillator strengths are generally higher than in absorption, ranging from 3.6426 (Chain 7) to 4.0039 (Chain 23). The increase in oscillator strength during emission suggests that these PPE chains have highly efficient radiative relaxation processes, meaning that a significant portion of the excited-state energy is released as fluorescence rather than being lost through non-radiative decay. Chain 23, with the highest oscillator strength (4.0039), is expected to exhibit the brightest fluorescence, whereas Chain 7, with the lowest oscillator strength (3.6426), might have slightly weaker fluorescence intensity compared to the others.

3.3.4 HOMO–LUMO contribution. The HOMO–LUMO contribution percentage represents how much of the electronic excitation is derived purely from a HOMO to LUMO transition, rather than involving other molecular orbitals. A high HOMO–LUMO contribution percentage means that the excitation is well-defined and primarily involves these frontier orbitals, leading to predictable optical properties. For absorption, most PPE chains exhibit a HOMO–LUMO contribution above 90%, with the highest contributions seen in Chain 18 (96.22%) and Chain 30 (96.06%). These high values suggest that the electronic transition in these chains is very localized to the HOMO and LUMO, meaning that their fluorescence properties are less influenced by other excited-state interactions or configurations. During fluorescence emission, the HOMO–LUMO contribution percentage further increases, ranging from 95.58% (Chain 23) to 97.09% (Chain 20). The increase in HOMO–LUMO contribution percentage suggests that the $S_1 \rightarrow S_0$ transitions are electronically well-defined and primarily involve frontier orbitals. However, this does not directly imply the suppression of non-radiative pathways, as the nature of excited-state decay involves additional dynamic and environmental factors beyond orbital composition.

3.3.5 HOMO, LUMO energies and energy gaps. The HOMO and LUMO energy levels determine the electronic transition characteristics and the overall stability of the molecular system. The HOMO energy values range from −5.693 eV (Chain 30) to −5.482 eV (Chain 29), indicating variations in electron-donating ability. A lower HOMO energy means the molecule is less prone to electron loss (oxidation), while a higher HOMO energy suggests easier electron donation. The LUMO energies vary from −2.087 eV (Chain 30) to −1.966 eV (Chain 11), with a more negative LUMO indicating stronger electron-accepting ability. The HOMO–LUMO energy gap is a crucial parameter, as a smaller gap generally leads to red-shifted absorption and emission due to lower excitation energy requirements. Chain 11

exhibits the largest HOMO–LUMO gap (3.666 eV), which corresponds to its highest excitation energy (2.8066 eV) and shortest absorption wavelength (441.75 nm). In contrast, Chain 29 has the smallest gap (3.499 eV), associated with a lower excitation energy (2.6897 eV) and a longer absorption wavelength (460.95 nm) In the fluorescence emission state, the HOMO–LUMO gaps decrease significantly due to excited-state relaxation effects. The HOMO–LUMO gap at the excited-state optimized geometry range from 2.807 eV (Chain 29) to 2.892 eV (Chain 18), meaning that excited-state molecules have a smaller energy gap than in the ground-state absorption phase. This energy gap reduction accounts for the Stokes shift, where emission occurs at a lower energy than absorption, consistent with structural relaxation in the excited state. While smaller gaps correlate with red-shifted fluorescence, we avoid inferring their effect on radiative *versus* non-radiative decay efficiency, as such dynamics depend on complex vibronic interactions not captured in the current study.

3.3.6 HOMO–LUMO orbital analysis. The HOMO–LUMO orbitals are essential in defining the electronic and fluorescence characteristics of PPE conjugated polymers. To analyze this, we extracted the HOMO and LUMO distributions of selected PPE dimer molecules from TD-DFT calculations for both absorption and emission, as illustrated in Fig. 5 (representative example) and SI Fig. S6–S11.

The HOMO and LUMO distributions reveal significant electron delocalization along the polymer backbone, a hallmark of PPE-type molecules. This extensive π-conjugation promotes efficient charge transfer and improves optical properties, including absorption and fluorescence. In the HOMO orbitals, bonding interactions occur between the two ethylene carbon atoms, while antibonding interactions are observed between a phenyl carbon and an ethylene carbon (single bond) or an oxygen atom in the side chain (single bond). The LUMO orbitals exhibit the opposite pattern, with bonding interactions localized between a phenyl carbon and an ethylene carbon (single bond) and antibonding interactions between the two ethylene carbons. These findings confirm that the HOMO–LUMO transition corresponds to a $\pi \rightarrow \pi^*$ excitation. Additionally, both HOMO and LUMO orbitals show charge transfer from the terminal phenyl group to the ethylene unit. As the molecular chain lengthens, the electron density becomes increasingly concentrated at the center of the backbone, suggesting conjugation saturation.

3.3.7 Absorption, emission spectra, and Stokes shifts. From the Gaussian TD-DFT calculations, we analyzed the absorption and emission spectra of selected PPE dimer chains, along with their Stokes shifts, as illustrated in Fig. 6, SI Fig. S12, S13 and Table S2. As depicted in Fig. 6, Fig. S12, S13 and

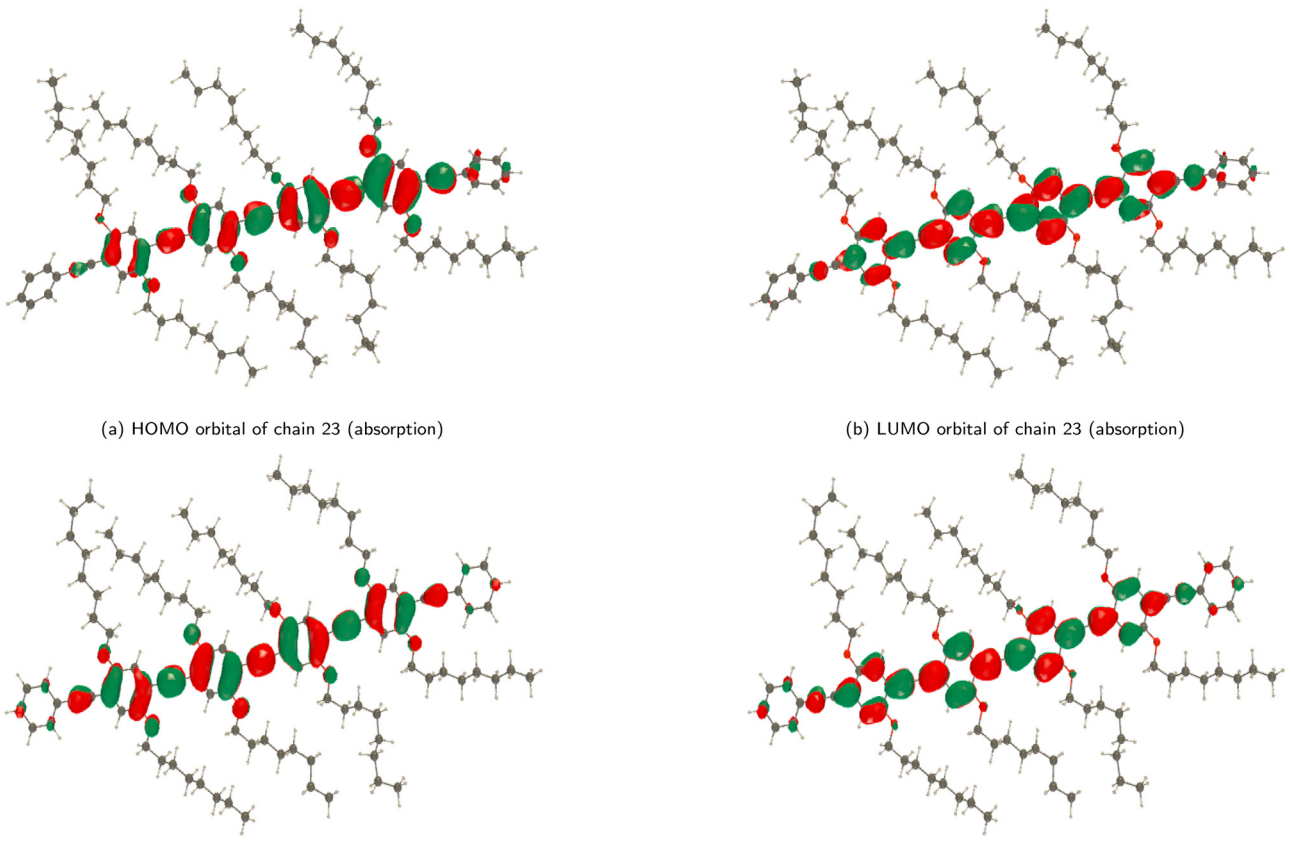

(a) HOMO orbital of chain 23 (absorption)

(b) LUMO orbital of chain 23 (absorption)

(c) HOMO orbital of chain 23 (emission)

(d) LUMO orbital of chain 23 (emission)

Fig. 5 The representative illustrations depict the HOMO and LUMO orbitals responsible for the absorption and emission of chain 23 of the PPE nanoparticle. These orbitals were calculated using TD-DFT.

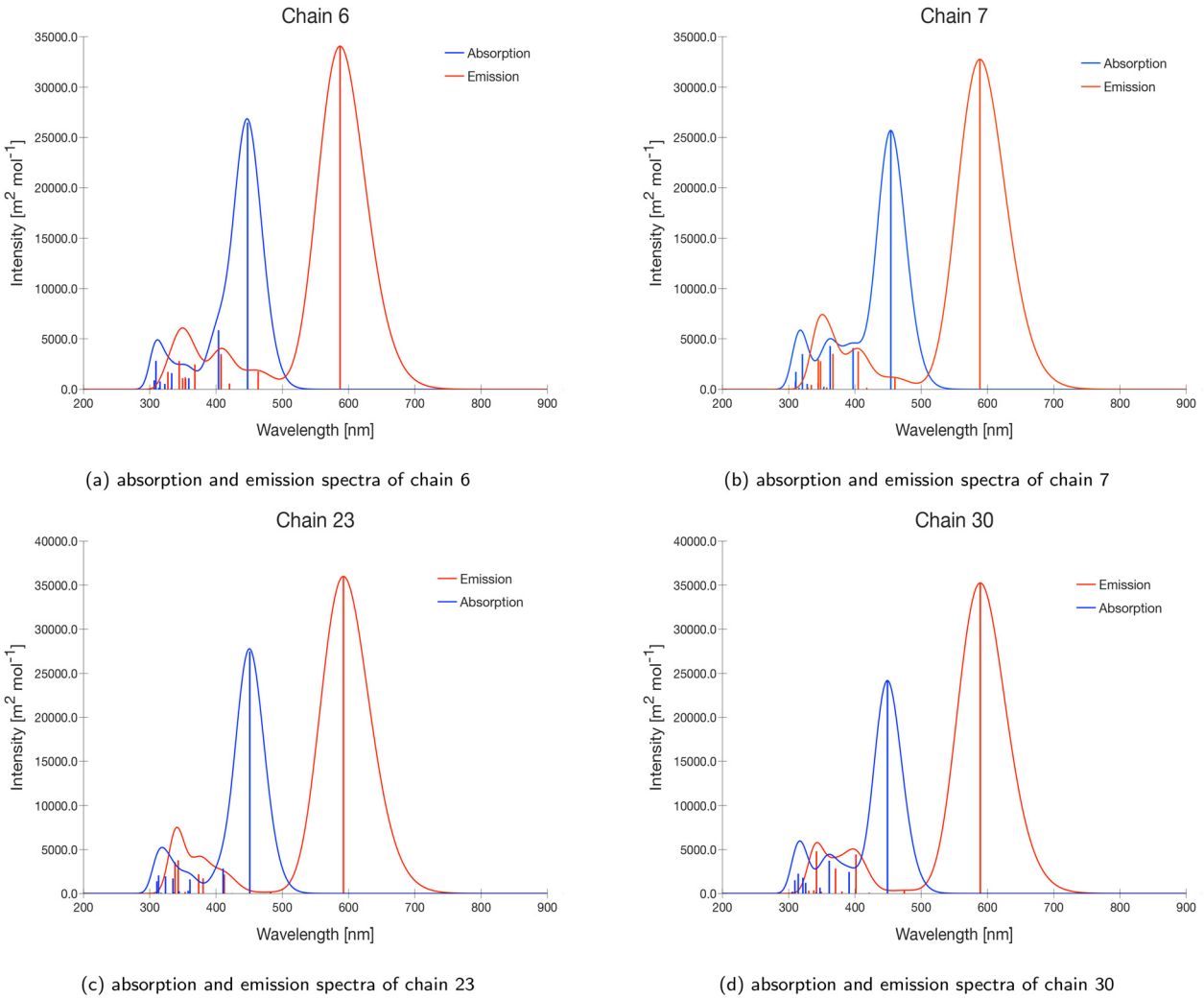

(a) absorption and emission spectra of chain 6

(b) absorption and emission spectra of chain 7

(c) absorption and emission spectra of chain 23

(d) absorption and emission spectra of chain 30

Fig. 6 Illustrations depict the UV spectra of absorption and emission for chain 6, 7, 23, and 30. These UV spectra were calculated using the TD-M05/6-31G(d,p) level of theory. The spectra were drawn using Gaussian broadening with a full width at half maximum (FWHM) factor of 0.3. Vertical blue and red straight lines signify the oscillator strength.

Table S2, the absorption spectra (blue) and emission spectra (red) of the selected PPE chains exhibit distinct peaks. The absorption spectra display peaks within the 441.75–460.95 nm range, while the emission spectra fall between 582.17–603.76 nm. Experimentally, the absorption and emission wavelengths were observed at 450 nm and 579 nm, respectively.

Stokes shift analysis provides insights into energy loss mechanisms, including vibrational relaxation and solvation effects. Defined as the difference between absorption and emission maxima, the Stokes shift values for PPE chains range from 134.51 nm (Chain 7) to 156.31 nm (Chain 11). The experimental Stokes shift is 129 nm, which is lower than most computed values, suggesting that the computational model predicts greater energy relaxation than observed experimentally. Chains 11 (156.31 nm), 28 (151.48 nm), and 20 (149.91 nm) exhibit the highest Stokes shifts, indicating significant non-radiative relaxation processes.

In terms of spectral trends and fluorescence properties, most chains exhibit red-shifted emission compared to the experimental value (579 nm), implying that the theoretical models may overestimate electronic relaxation effects. Chain 29, with an absorption peak at 460.95 nm and an emission peak at 603.76 nm, displays the most red-shifted values, suggesting enhanced electronic conjugation. Chains with higher Stokes shifts (*e.g.*, Chain 11, 20, 28, and 29) may experience greater intramolecular charge transfer (ICT) effects or stronger environmental interactions, leading to increased energy dissipation. Additionally, the emission spectra are consistently broader than the absorption spectra, a typical characteristic due to relaxation and the distribution of excited-state conformations.

Comparing computational and experimental data, most chains exhibit absorption peaks (445–460 nm) slightly higher than the experimental value (450 nm), indicating that the theoretical model slightly overestimates transition energy. Similarly, computed emission peaks are generally red-shifted

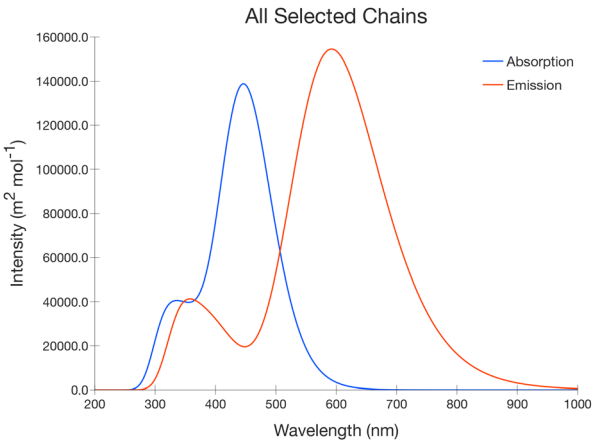

Fig. 7 Illustration depicts the combined UV spectra of absorption and emission for chain 6, 7, 11, 18, 20, 23, 28, 29, and 30. The UV spectra were calculated using the TD-M05/6-31G(d,p) level of theory. The spectra were drawn using Gaussian broadening with a full width at half maximum (FWHM) factor of 0.6.

relative to the experimental value (579 nm), possibly due to solvation effects or electronic-state interactions not fully captured in the theoretical framework. The experimental Stokes shift (129 nm) is at the lower end of the computed range, further supporting the idea that theoretical predictions may overestimate vibrational relaxation.

To further examine the overall absorption and emission characteristics of the nanoparticle, we combined the spectra of selected PPE chains, as presented in Fig. 7. The average computed absorption and emission wavelengths were 449.10 nm and 592.68 nm, respectively, with an average Stokes shift of 143.59 nm. These findings indicate that the computational average absorption wavelength closely aligns with the experimental value, whereas the computational emission wavelength is slightly overestimated compared to the experimental PPE nanoparticle emission wavelength.

3.3.8 Bond length alternation (BLA). To investigate the structure–property relationships governing the optoelectronic performance of PPE nanoparticles, we analyzed the bond length alternation (BLA) values of ethynylene groups that linked phenylene groups for selected chains (Chains 6, 7, 11, 18, 20, 23, 28, 29, and 30). BLA was determined by quantifying the difference in bond lengths among the three carbon atoms within each ethynylene linker group for both absorption and emission geometries. The acetylene bond (sp-hybridized carbon triple bond) was chosen for BLA analysis because it forms the central linker between phenylene units in PPE and plays a crucial role in π-conjugation. Changes in this bond length serve as a sensitive indicator of electronic delocalization and excited-state structural relaxation in the dimer chains. For each ethynylene group, two BLA measurements were made: (1) C≡C–C oriented toward the left phenylene ring ($EG1_L$) and (2) C≡C–C oriented toward the right phenylene ring ($EG1_R$). Each chain contains five ethynylene linkages, resulting in a total of ten BLA values per chain. Fig. 8 illustrates the structure of a PPE chain,

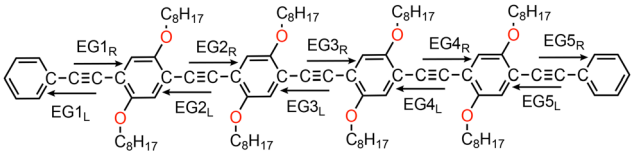

Fig. 8 Structure of the PPE dimer chain showing the ethynylene groups (EGs) and bond length alternation (BLA) measurement groups. The chain contains five EG groups (EG1 to EG5), each comprising two BLA measurement regions indicated with left and right arrows—for example, $EG1_L$ (left) and $EG1_R$ (right) for EG1.

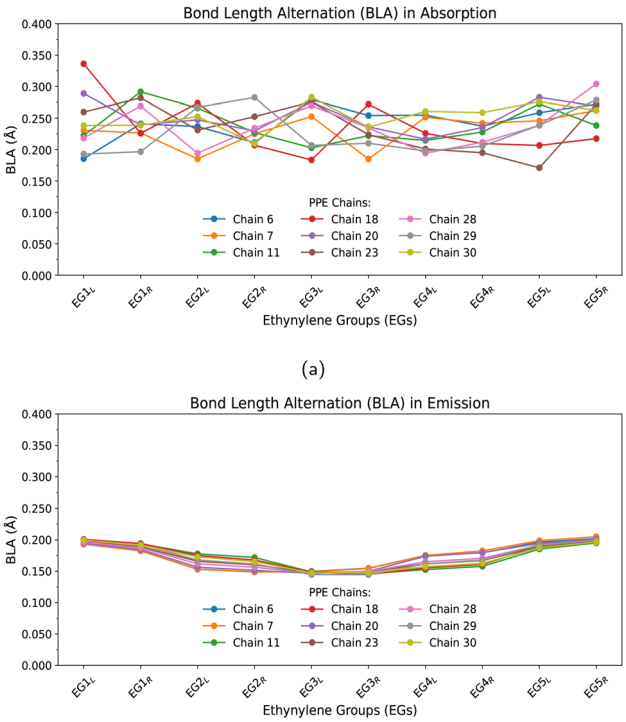

Fig. 9 Depiction of bond length alternation (BLA, in Å) measurements for the ethynylene groups in selected PPE chains during (a) absorption and (b) emission. Each PPE chain comprises five ethynylene group (EG) units (EG1–EG5), with two BLA measurement regions per unit, designated as left (L) and right (R)—for example, $EG1_L$ and $EG1_R$.

highlighting ethynylene groups (EGs) and the corresponding BLA measurements groups. Fig. 9 and SI Table S3 present the BLA values of ethynylene groups for selected chains of PPE nanoparticles for both absorption and emission. These values were then correlated with TD-M05/6-31G(d,p)-calculated photophysical properties, including vertical excitation energy, oscillator strength, HOMO–LUMO energy gap, and fluorescence emission wavelengths (Table 2).

In general, chains exhibiting lower BLA values demonstrate greater conjugation and structural delocalization, which are known to facilitate red-shifted electronic transitions and enhance oscillator strength. For example, Chain 11 shows one of the lowest average BLA values across both EG1 and EG2

Table 2 The table shows the vertical excitation lengths (compared with experimental[9] value), vertical excitation energies, oscillator strengths, HOMO–LUMO contribution percentages, HOMO energies, LUMO energies, and HOMO–LUMO energy gaps for the highest-energy excited state of selected PPE dimer chains, performed using TD-M05/6-31G(d,p) level of theory

PPE Chains	Vertical excitation length (nm)	Vertical excitation energy (eV)	Oscillator strength (f)	HOMO–LUMO contribution (%)	HOMO energy (eV)	LUMO energy (eV)	HOMO–LUMO energy Gap (eV)
Absorption							
Chain 6	447.60	2.770	2.946	83.10	−5.589	−2.033	3.556
Chain 7	454.12	2.730	2.855	94.98	−5.559	−1.983	3.576
Chain 11	441.75	2.807	2.698	94.90	−5.632	−1.966	3.666
Chain 18	446.03	2.780	3.140	96.22	−5.662	−2.035	3.627
Chain 20	445.09	2.786	2.994	94.19	−5.683	−2.032	3.651
Chain 23	450.94	2.750	3.058	88.65	−5.632	−2.048	3.584
Chain 28	446.33	2.778	3.241	92.83	−5.683	−2.070	3.613
Chain 29	460.95	2.690	2.983	91.02	−5.482	−1.983	3.499
Chain 30	449.05	2.761	2.689	96.06	−5.693	−2.087	3.606
Experimental[9]	450.00	—	—	—	—	—	—
Emission							
Chain 6	587.21	2.111	3.788	97.02	−5.186	−2.328	2.858
Chain 7	588.63	2.106	3.643	97.03	−5.179	−2.319	2.860
Chain 11	598.06	2.073	3.797	97.06	−5.145	−2.329	2.816
Chain 18	582.17	2.130	3.781	96.71	−5.235	−2.343	2.892
Chain 20	595.00	2.084	3.787	97.09	−5.146	−2.316	2.830
Chain 23	592.34	2.093	4.004	95.58	−5.153	−2.311	2.842
Chain 28	597.81	2.074	3.934	96.58	−5.142	−2.319	2.823
Chain 29	603.76	2.053	3.789	96.68	−5.130	−2.307	2.807
Chain 30	589.16	2.104	3.921	96.09	−5.187	−2.332	2.855
Experimental[9]	579.00	—	—	—	—	—	—

segments, particularly in the emission state (*e.g.*, $EG3_R$ = 0.1767 Å), and concurrently exhibits high oscillator strength (f = 3.7974) and strong conjugation, as reflected by its low HOMO–LUMO gap (2.816 eV) and red-shifted emission (598.06 nm). Similarly, Chain 30, with consistently low BLA values in both the absorption and emission states ($EG1_L$ = 0.1936 Å; $EG4_L$ = 0.1873 Å), demonstrates a notably high HOMO–LUMO contribution (96.06%) and red-shifted emission at 589.16 nm, underscoring enhanced electron delocalization. In contrast, Chain 6, which shows relatively larger BLA values across multiple ethynylene units (*e.g.*, $EG1_L$ = 0.1931 Å, $EG3_R$ = 0.1642 Å), exhibits a blue-shifted emission at 587.21 nm, a larger HOMO–LUMO gap (2.858 eV), and a lower oscillator strength (f = 3.7881) compared to Chain 11 or Chain 30. This suggests that increased bond length alternation restricts π-conjugation, thereby raising excitation energy and decreasing fluorescence efficiency.

Interestingly, the BLA values tend to decrease upon relaxation to the emission geometry for most chains, indicative of increased delocalization in the excited state. For instance, Chain 23 shows a transition from a relatively high BLA in absorption ($EG1_L$ = 0.2702 Å) to a lower BLA in emission ($EG1_L$ = 0.1872 Å), which corresponds with a significant increase in oscillator strength (f = 4.0039) and a modest HOMO–LUMO gap (2.842 eV), resulting in a red-shifted emission (592.34 nm). This structural relaxation toward more delocalized geometries likely contributes to enhanced radiative decay pathways and fluorescence efficiency. Furthermore, the degree of symmetry in BLA values across ethynylene units (*i.e.*, between $EG1_L$ and $EG1_R$, $EG2_L$ and $EG2_R$, *etc.*) also correlates with orbital purity and localization. Chains with highly symmetric and small BLA values, such as Chain 18 and Chain 30, exhibit high HOMO–LUMO contributions (96.22% and 96.06%, respectively), indicating that the lowest-energy excitation is dominated by a single frontier orbital transition. These chains also demonstrate more intense absorption bands and greater oscillator strengths, making them promising candidates for efficient light-harvesting or emissive materials.

Despite general trends, some outliers such as Chain 29, which shows relatively high BLA asymmetry (*e.g.*, $EG2_L$ = 0.1954 Å *vs.* $EG2_R$ = 0.1619 Å in emission), still maintains a strong oscillator strength (f = 3.8886) and red-shifted emission (603.76 nm). This indicates that local geometry and electronic effects, including torsional angles and side-chain interactions, may also influence conjugation and photophysical behavior beyond BLA alone. This analysis demonstrates that lower bond length alternation and increased geometric symmetry correlate strongly with enhanced fluorescence properties in PPE nanoparticles. Chains that exhibit delocalized π-electron structures in both absorption and emission states show stronger oscillator strengths, reduced HOMO–LUMO gaps, and red-shifted fluorescence, underscoring the utility of BLA as a predictive structural parameter in the design of conjugated polymer materials.

Overall, PPE nanoparticles and their constituent dimer chains exhibit highly promising fluorescence properties, making them strong candidates for bio-imaging and other fluorescence-based applications. Molecular dynamics (MD) simulations revealed that PPE nanoparticles, composed of 30 dimer chains, maintain structural stability in aqueous environments by forming a uniform spherical shape through van der Waals and electrostatic interactions. Notably, the hydrophobic

octyloxy side chains prevent water penetration into the nanoparticle core, ensuring stability—a crucial feature for biological applications where water resistance minimizes fluorescence quenching and degradation. The study employed time-dependent density functional theory (TD-DFT) to accurately predict the optical properties of PPE systems. Among several tested functionals, the M05 hybrid functional provided the closest match to experimental absorption wavelengths (450.94 nm *vs.* 450.00 nm), demonstrating its reliability for modeling PPEs electronic transitions. This functional also correctly predicted key fluorescence parameters, including excitation energies, oscillator strengths, and HOMO–LUMO contributions, which are essential for understanding PPEs light-emitting behavior. The high oscillator strengths observed (ranging from 2.689 to 4.004) indicate strong absorption and bright fluorescence, a critical requirement for sensitive detection in bio-imaging. Further analysis of individual PPE dimer chains revealed excellent fluorescence characteristics, including well-defined absorption (441.75–460.95 nm) and emission peaks (582.17–603.76 nm). The significant Stokes shift (129–156 nm) between absorption and emission reduces spectral overlap, minimizing self-quenching and improving signal clarity in imaging applications. Additionally, the dominance of HOMO–LUMO transitions (>90%) suggests that PPE chains exhibit predictable and efficient $\pi \rightarrow \pi^*$ electronic transitions, further enhancing their suitability as fluorescent probes. The hydrophobic nature of the nanoparticles, combined with their bright and stable fluorescence, positions them as ideal candidates for long-term cellular or tissue imaging.

4 Conclusion

This research undertook a computational exploration of poly(*p*-phenylene ethynylene) nanoparticles (PPE-NPs), investigating their potential as advanced bio-imaging probes by utilizing their distinctive optical properties. Through the integration of molecular dynamics (MD) simulations and time-dependent density functional theory (TD-DFT) calculations, the study aimed to predict and verify the fluorescence characteristics of PPE-NPs, encompassing absorption and emission spectra, Stokes shifts, and electronic transitions. The investigation evaluated six hybrid functionals to ascertain the most precise computational method for forecasting optical properties, with the M05 functional being identified as the optimal choice. Furthermore, the structural stability of PPE-NPs in aqueous environments was assessed to determine their feasibility for biological applications. The principal findings of this research are as follows:

- The M05 hybrid functional provided the closest match to experimental absorption wavelengths (450.94 nm *vs.* 450.00 nm), demonstrating its reliability for modeling PPE-NPs' electronic transitions.
- PPE-NPs exhibited strong fluorescence with high oscillator strengths (2.689–4.004), indicating bright and efficient light emission, ideal for sensitive bio-imaging.
- The hydrophobic octyloxy side chains of PPE-NPs prevented water penetration into the nanoparticle core, ensuring structural stability and minimizing fluorescence quenching in biological environments.
- A significant Stokes shift (129–156 nm) was observed between absorption and emission, reducing spectral overlap and enhancing signal clarity for imaging applications.
- HOMO–LUMO analysis revealed dominant $\pi \rightarrow \pi^*$ transitions (>90% contribution), confirming predictable and efficient electronic behavior in PPE-NPs.
- Lower bond length alternation (BLA) and greater geometric symmetry in ethynylene linkages of PPE chains strongly correlate with enhanced π-conjugation, leading to red-shifted emission, higher oscillator strength, and reduced HOMO–LUMO gaps—making BLA a valuable structural descriptor for optimizing optoelectronic properties in conjugated polymer nanoparticles.

These computational insights suggest that PPE-NPs exhibit optical and structural features highly compatible with biological imaging, including emission in the visible range (582–604 nm), aqueous stability, and strong oscillator strengths. Their compact size and photostable characteristics support potential use in fluorescence-based biosensing and cellular labeling applications.

The findings of this study underscore the promise of PPE-NPs as robust and adaptable fluorescent probes for bio-imaging, attributable to their adjustable optical properties, structural durability, and intense emission. The computational framework developed herein validates experimental results while also serving as a predictive tool for the design of next-generation conjugated polymer nanoparticles with specific imaging applications in mind. This research emphasizes the significance of integrating computational and experimental methodologies to advance the development of materials for biomedical applications, unlocking new opportunities for high-resolution, prolonged imaging in both diagnostic and therapeutic contexts.

While our computational approach provides valuable insights, some limitations should be acknowledged. The use of PPE dimers may not capture the full extent of long-range delocalization in larger polymer chains. TD-DFT, although widely used, has inherent accuracy limits for excitation energies. Additionally, biological media were not explicitly modeled, and future studies could incorporate protein interactions or cellular environments to further validate PPE-NP bioimaging potential.

Author contributions

Anupom Roy: all computational calculations, and writing; Conrard Giresse Tetsassi Feugmo: initial MD simulations, supervision, review, and editing.

Conflicts of interest

There are no conflicts to declare.

Data availability

All MD simulations and DFT calculations data are available at: https://zenodo.org/doi/10.5281/zenodo.17054528.

Supplementary information: Fig. S1–S5: conformational changes of all 30 chains of PPE nanoparticle at 4000 ns MD simulation. Table S1: absorption data of 30 chains. Fig. S6–S8: HOMO–LUMO orbitals of selected chains for absorption. Table S2: absorption and emission wavelength and Stokes shift. Fig. S9–S11: HOMO–LUMO orbitals of selected chains for emission. Fig. S12 and S13: TD-DFT calculated absorption and emission spectra of selected chains. Table S3: bond length alternation (BLA) values of ethynylene groups of all selected chains. See DOI: https://doi.org/10.1039/d5tb00890e

Acknowledgements

C. G. Tetsassi Feugmo extends sincere appreciation to the University of Waterloo for the Start-up Grant, which substantially contributed to the progression of this research by facilitating access to critical resources and promoting collaborative endeavors. This work was made possible by the facilities of the Shared Hierarchical Academic Research Computing Network (SHARCNET:www.sharcnet.ca) and Digital Research Alliance of Canada (https://alliancecan.ca/en).

References

1 Z. Sun, K. Ng and N. Ramli, *Biomed. Imaging Intervention J.*, 2011, **7**, e21.
2 R. Weissleder, *Science*, 2006, **312**, 1168–1171.
3 G. P. Drummen, *Molecules*, 2012, **17**, 14067–14090.
4 J. W. Lichtman and J.-A. Conchello, *Nat. Methods*, 2005, **2**, 910–919.
5 J. Rao, A. Dragulescu-Andrasi and H. Yao, *Curr. Opin. Biotechnol*, 2007, **18**, 17–25.
6 S. A. Hilderbrand and R. Weissleder, *Curr. Opin. Chem. Biol.*, 2010, **14**, 71–79.
7 C. Wu and D. T. Chiu, *Angew. Chem., Int. Ed.*, 2013, **52**, 3086–3109.
8 Y. Braeken, S. Cheruku, A. Ethirajan and W. Maes, *Materials*, 2017, **10**, 1420.
9 L. D'Olieslaeger, Y. Braeken, S. Cheruku, J. Smits, M. Ameloot, D. Vanderzande, W. Maes and A. Ethirajan, *J. Colloid Interface Sci.*, 2017, **504**, 527–537.
10 Y. Braeken, S. Cheruku, S. Seneca, N. Smisdom, L. Berden, L. Kruyfhooft, H. Penxten, L. Lutsen, E. Fron and D. Vanderzande, *et al.*, *ACS Biomater. Sci. Eng.*, 2019, **5**, 1967–1977.
11 H. Sun, D. Martinez, Z. Li and K. S. Schanze, *ACS Appl. Mater. Interfaces*, 2020, **12**, 53310–53317.
12 D. Tuncel and H. V. Demir, *Nanoscale*, 2010, **2**, 484–494.
13 M. Tsakama, X. Ma, Y. He, W. Chen and X. Dai, *Molecules*, 2018, **23**, 2056.
14 S. Dellsperger, F. Dötz, P. Smith and C. Weder, *Macromol. Chem. Phys.*, 2000, **201**, 192–198.
15 I. Barboza-Ramos, H. B. Gobeze, D. Wherritt and K. S. Schanze, *Macromolecules*, 2024, **57**, 7575–7585.
16 K. Kokado and Y. Chujo, *Polym. J.*, 2010, **42**, 363–367.
17 J. H. Moon and T. M. Swager, *Macromolecules*, 2002, **35**, 6086–6089.
18 C.-H. Shu, M.-X. Liu, Z.-Q. Zha, J.-L. Pan, S.-Z. Zhang, Y.-L. Xie, J.-L. Chen, D.-W. Yuan, X.-H. Qiu and P.-N. Liu, *Nat. Commun.*, 2018, **9**, 2322.
19 M. Elter, M. Brosz, D. Sucerquia, A. Kuzhelev, D. C. Kiesewetter, M. Kurth, A. Dreuw, T. F. Prisner, J. Freudenberg and U. H. Bunz, *et al.*, *J. Am. Chem. Soc.*, 2024, **146**, 27594–27599.
20 M. Orio, D. A. Pantazis and F. Neese, *Photosynth. Res.*, 2009, **102**, 443–453.
21 S. A. Hollingsworth and R. O. Dror, *Neuron*, 2018, **99**, 1129–1143.
22 O. C. Adekoya, G. J. Adekoya, E. R. Sadiku, Y. Hamam and S. S. Ray, *Pharmaceutics*, 2022, **14**, 1972.
23 H. Piwoński, S. Nozue and S. Habuchi, *ACS Nanosci. Au*, 2022, **2**(4), 253–283.
24 V. Liegeois, DrawMol, https://www.unamur.be/drawmol, UNamur.
25 E. Cances, B. Mennucci and J. Tomasi, *J. Chem. Phys.*, 1997, **107**, 3032–3041.
26 M. J. Frisch, G. W. Trucks, H. B. Schlegel, G. E. Scuseria, M. A. Robb, J. R. Cheeseman, G. Scalmani, V. Barone, G. A. Petersson, H. Nakatsuji, X. Li, M. Caricato, A. V. Marenich, J. Bloino, B. G. Janesko, R. Gomperts, B. Mennucci, H. P. Hratchian, J. V. Ortiz, A. F. Izmaylov, J. L. Sonnenberg, D. Williams-Young, F. Ding, F. Lipparini, F. Egidi, J. Goings, B. Peng, A. Petrone, T. Henderson, D. Ranasinghe, V. G. Zakrzewski, J. Gao, N. Rega, G. Zheng, W. Liang, M. Hada, M. Ehara, K. Toyota, R. Fukuda, J. Hasegawa, M. Ishida, T. Nakajima, Y. Honda, O. Kitao, H. Nakai, T. Vreven, K. Throssell, J. A. Montgomery, Jr., J. E. Peralta, F. Ogliaro, M. J. Bearpark, J. J. Heyd, E. N. Brothers, K. N. Kudin, V. N. Staroverov, T. A. Keith, R. Kobayashi, J. Normand, K. Raghavachari, A. P. Rendell, J. C. Burant, S. S. Iyengar, J. Tomasi, M. Cossi, J. M. Millam, M. Klene, C. Adamo, R. Cammi, J. W. Ochterski, R. L. Martin, K. Morokuma, O. Farkas, J. B. Foresman and D. J. Fox, *Gaussian ~ 16 Revision C.01*, Gaussian Inc., Wallingford CT, 2016.
27 L. Martnez, R. Andrade, E. G. Birgin and J. M. Martnez, *J. Comput. Chem.*, 2009, **30**, 2157–2164.
28 C. I. Bayly, P. Cieplak, W. Cornell and P. A. Kollman, *J. Phys. Chem.*, 1993, **97**, 10269–10280.
29 A. Fortuna, P. M. Suzano, M. Machuqueiro and P. J. Costa, *J. Comput. Biophys. Chem.*, 2024, **23**, 481–491.
30 J. C. Meza, *Wiley Interdiscip. Rev.: Comput. Mol. Sci.*, 2010, **2**, 719–722.
31 M. Parrinello and A. Rahman, *Method J. Appl. Phys.*, 1981, **52**, 7182–7190.
32 T. Darden, D. York and L. Pedersen, *et al.*, *J. Chem. Phys.*, 1993, **98**, 10089.

33 H. Berendsen, D. van der Spoel and R. van Drunen, *Comput. Phys. Commun.*, 1995, **91**, 43–56.
34 D. Van Der Spoel, E. Lindahl, B. Hess, G. Groenhof, A. E. Mark and H. J. C. Berendsen, *J. Comput. Chem.*, 2005, **26**, 1701–1718.
35 B. Hess, C. Kutzner, D. van der Spoel and E. Lindahl, *J. Chem. Theory Comput.*, 2008, **4**, 435–447.
36 W. L. Jorgensen, D. S. Maxwell and J. Tirado-Rives, *J. Am. Chem. Soc.*, 1996, **118**, 11225–11236.
37 S. Jo, T. Kim, V. G. Iyer and W. Im, *J. Comput. Chem.*, 2008, **29**, 1859–1865.
38 A. D. Becke, *J. Chem. Phys.*, 1993, **98**, 5648–5652.
39 C. Lee, W. Yang and R. G. Parr, *Phys. Rev. B: Condens. Matter Mater. Phys.*, 1988, **37**, 785.
40 J.-D. Chai and M. Head-Gordon, *Phys. Chem. Chem. Phys.*, 2008, **10**, 6615–6620.
41 T. Yanai, D. P. Tew and N. C. Handy, *Chem. Phys. Lett.*, 2004, **393**, 51–57.
42 Y. Zhao, N. E. Schultz and D. G. Truhlar, *J. Chem. Phys.*, 2005, **123**, 161103–161106.
43 Y. Zhao and D. G. Truhlar, *Theor. Chem. Acc.*, 2008, **120**, 215–241.
44 R. Peverati and D. G. Truhlar, *J. Phys. Chem. Lett.*, 2011, **2**, 2810–2817.